Supporting Information

Laminar Flow-Assisted Synthesis of Amorphous ZIF-8 Based Nano-motor with Enhanced Transmigration for Photothermal Cancer Therapy

Byung Kwon Kaang, Laura Ha, Jeong-Un Joo and Dong-Pyo Kim*

Experimental section

1. Fabrication of a capillary reactor integrated with two 3D printed connectors

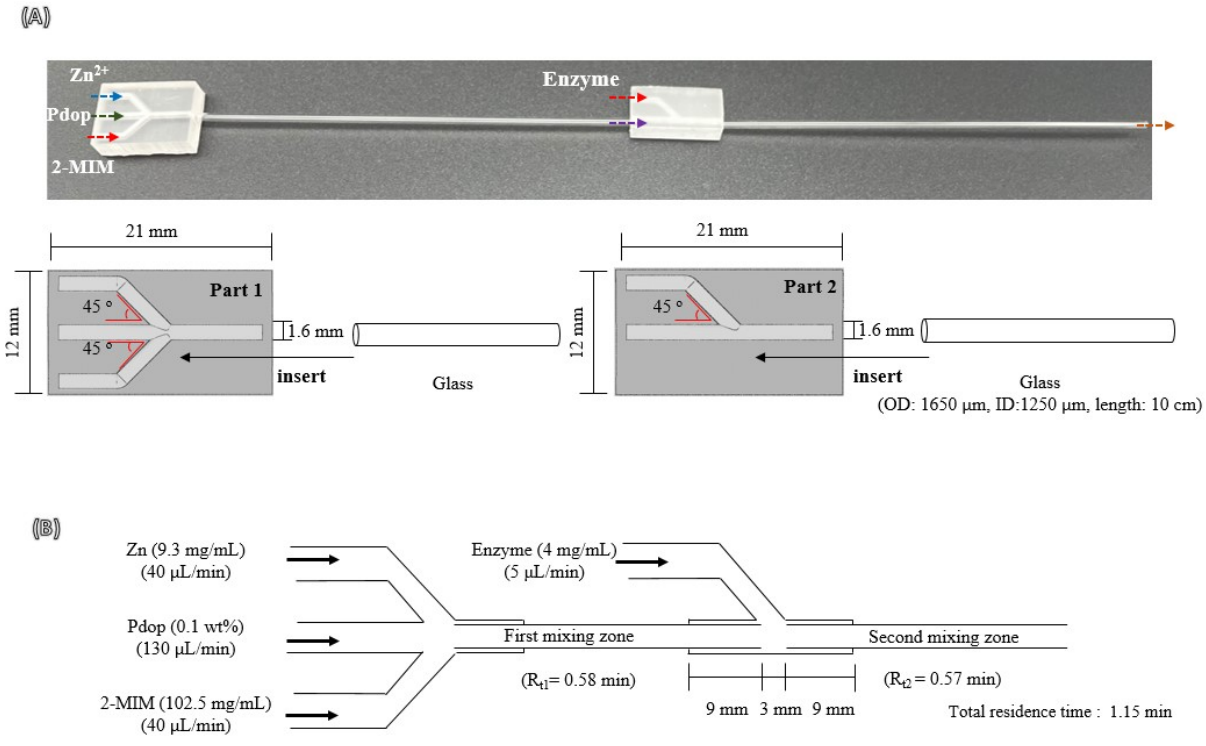

Fig. S1. (A) Actual image and (B) schematic illustration of flow reactor for synthesizing Pdop@enzyme@aZIF-8, which is composed of 2 pieces of glass capillary reactors (I.D: 1250 μm, length: 10 cm) and 2 pieces of three- and two-way 3D printed connectors (2.1 cm). The

glass capillary were 20 cm long in total by inserting up to 9 mm in both inlet and outlet of the 3D printed connectors.

The glass capillary reactor integrated to 3D printed connectors to synthesize Pdop@enzyme@aZIF-8 is shown in **Fig. S1**. The flow reactor (3D printed connector+glass capillary) consisted of 2 pieces of glass capillary (O.D: 1650 μm, I.D: 1250 μm, length: 10 cm) and 2 pieces of 3D printed three- and two-way connectors. Flow reactor was made very easily and reproducibly. 3D printed connector was used for connecting the glass capillary and injecting the each solution. And the glass capillary reactor was used for reaction of the Pdop@urease@amorphous ZIF-8. The laminar flow was readily generated in the rigid glass capillary part which preferably maintained the straight flow with high reproducibility, compared to using the flexible and readily curved plastic tube. The three and two-way 3D printed connectors were designed with auto-CAD software to create a virtual object (Autodesk inventor 2020). Then, connectors were printed with Digital Light Processing (DLP) desktop printer (Asiga Pico 2, Australia) with a UV-curable acrylate resin (Plas. CLEAR, ASIGA). Multiple digital masks were irradiated with UV (wavelengths: 385 nm and intensity: 2 mW/cm^2) during an exposure time of 5 sec with a set of layers 40 μm thick. Then they were washed repeatedly with isopropanol and ethanol to remove the uncured 3D printed resin. To obtain a more robust shape, they were post-treated with a UV radiation lamp with 2 mW/cm^2 intensity for 30 min. The three- and two-way connectors have the same transverse (21 mm), longitudinal (12 mm), and inner channel diameter (1.6 mm). The angles of the three- and two-way connector were 45°.

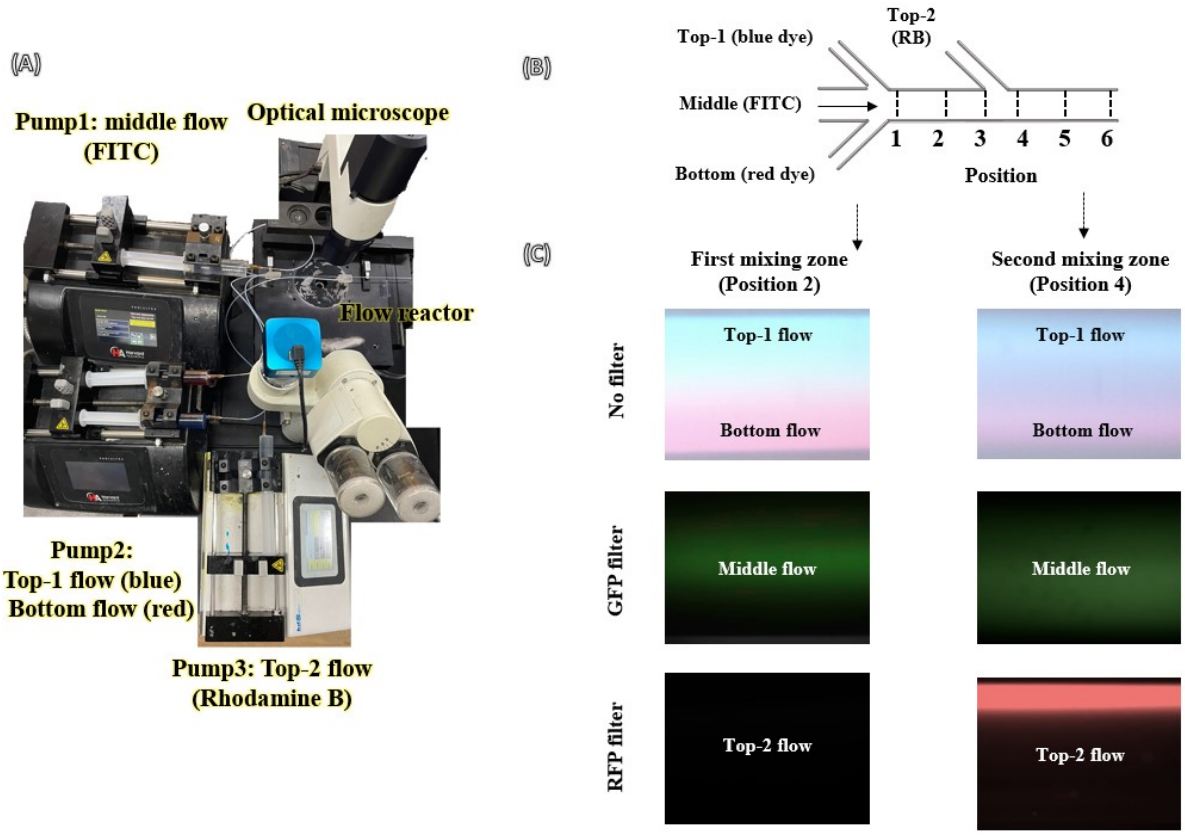

Fig. S2. Visualization of multiple laminar flow behavior using aqueous dying in the same capillary flow reactor used for the synthesis of Pdop@enzyme@ZIF-8. (A) Image of the laminar flow monitoring system euipped with optical microscopy. (B) Infusion of blue dye solution into top-1 inlet, FITC dye into middle inlet, red dye into bottom inlet, and rhodamine B (RB) dye into top-2 inlet, and six positions (#1 to 6) for measuring the color code, where are located at distance of 0.8 cm (#1), 5.6 cm (#2), 9 cm (#3), 11 cm (#4), 15.5 cm (#5), and 20 cm (#6) from the initial inlets. (C) Typical visual images taken by the monitoring system with no filter, GFP and RFP filters at the position #2 of first mixing zone and position #4 of second mixing zone under flow condition C2 (flow ratio, middle: top-2: (top-1+bottom) = 26: 1: 16, top-1/bottom = 1, 5 μL/min of top-2).

2. Degree of interfacial diffusion test with different laminar flows

2.1. Laminar flow monitoring using dying solutions

The degree of interfacial diffusion was calculated with a slight modification of the mixing efficiency calculation method [1,2]. Flow monitoring systems were identical to the synthetic systems of Pdop@enzyme@ZIF-8 in the glass channel, while several types of aqueous dying solutions, instead of actual reagents, were used to visualize the laminar flow behavior for quantifying the degree of interfacial diffusion **(Fig. S2)**. In typical, 4 inlets of bottom, top-1, middle and top-2 were used to infuse red dyed, blue dyed, FITC, and rhodamine B solutions.

2.2. Calculation of the degree of interfacial diffusion

First, six color images were attained at positions in the flow path (#1-6; distance: #1: 0.8 cm, #2: 5.6 cm, #3: 9 cm, #4: 11 cm, #5: 15.5 cm, and #6: 20 cm) with different flow conditions (C1-C3) by using optical microscope of flow monitoring system. Second, the numerical red color codes (ex. 0-255) of 6 longitudinal nodes where were vertically located at the horizontal flow positions in six color images were taken from the RGB images of PowerPoint of Microsoft by clicking “More color” in the color image, followed by choosing “Custom tab” in the dialog box to confirm red color code (***Table 1***). Note that similar numerical results were obtained no matter which color was selected. Third, standard deviations at different positions of flow path were calculated by following equation (***Table 2, equation 1***).

$$\sigma = \sqrt{\frac{1}{N}\sum_{l}^{N}(C_l - C_m)^2} \quad \cdots (1)$$

is the standard deviation of red color code value at 6 nodes, N is the number of nodes at a cross position, C_l is a red color code value of a certain node, C_m is the mean red color code value of 6 nodes.

$$\eta = (1 - \sqrt{\frac{\sigma^2}{\sigma_{initial}^2}}) \times 100 \quad \cdots (2)$$

is the degree of interfacial diffusion of at certain position (#1-6), $\sigma_{initial}$ and σ are the standard deviations of the initial position (#1) and the certain position under flow conditions (C1-C3).

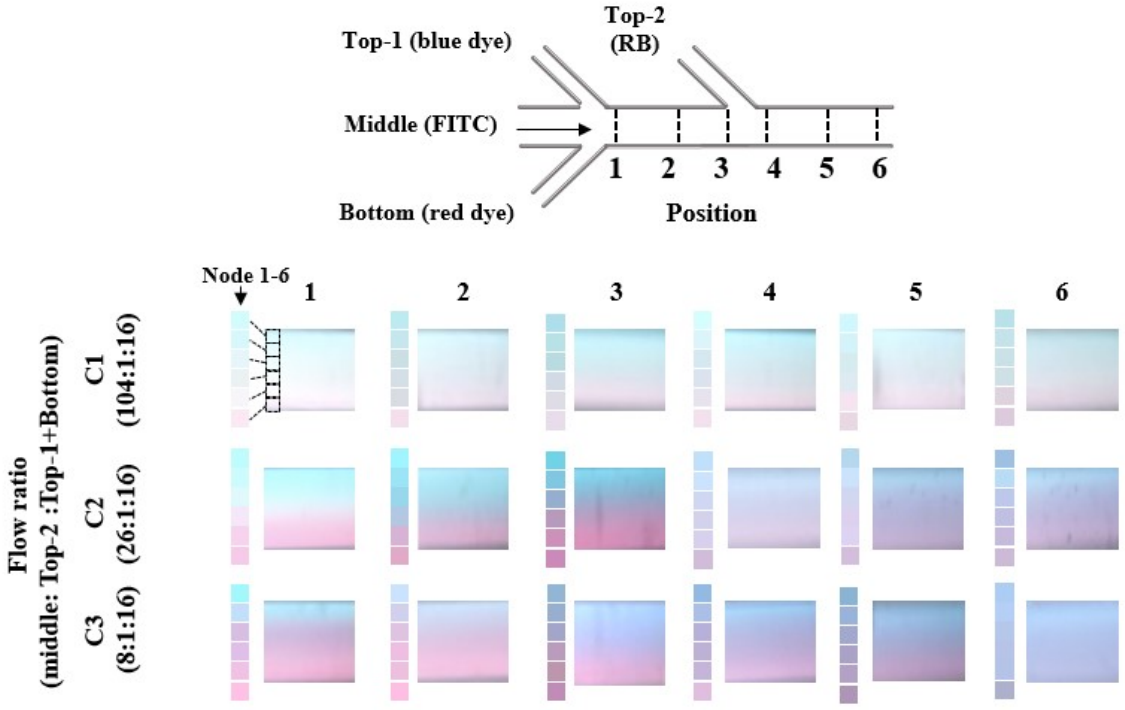

Fig. S3. Actual visual microscopic images of multiple liminar flow along positions (#1-#6) of flow path, taken by the monitoring system with no filter under three C1~C3 conditions with different ratios of middle: top-2: (top-1+bottom) flows. C1 = 104:1:16, C2 = 26:1:16, C3 = 8:1:16, top-1/bottom = 1, 5 μL/min of top-2. Note that the degree of interfacial diffusion was calculated by using numerical red color codes of 6 longitudinal nodes accoding to equation (1) and (2).

Table S1. Tyical example of numerical red color code obtained under flow condition C2 (middle: top-2: (top-1+bottom) = 26:1:16).

	Position 1	**Position 2**	**Position 3**	**Position 4**	**Position 5**	**Position 6**
Node 1	255	226	217	222	211	216
Node 2	254	215	215	220	198	211
Node 3	233	179	179	213	191	209
Node 4	200	153	165	209	190	207
Node 5	179	155	162	204	185	204
Node 6	164	160	162	169	162	175

Table S2. Calculated standard deviations at different positions of flow path under three flow conditions (C1-C3), by equation (1).

	Position 1	**Position 2**	**Position 3**	**Position 4**	**Position 5**	**Position 6**
C1	23.5	20.0	16.6	14.5	14.5	13.3
C2	38.8	31.8	26.0	19.4	16.2	14.6
C3	38.6	27.7	24.4	12.3	9.6	3.0

Table S3. Calculated degree of interfacial diffusion at different positions of flow path under three flow conditions (C1-C3), by equation (2).

	Position 1	**Position 2**	**Position 3**	**Position 4**	**Position 5**	**Position 6**
C1	0	14.6	29.1	38.1	38.3	43.4
C2	0	17.9	32.9	50.1	58.3	62.4
C3	0	28.2	36.6	67.9	75.1	92.1

Ex; degree of interfacial diffusion (position 2, C2): η=(1-√(31.8^2/(38.8^2)))×100 = 17.9 %

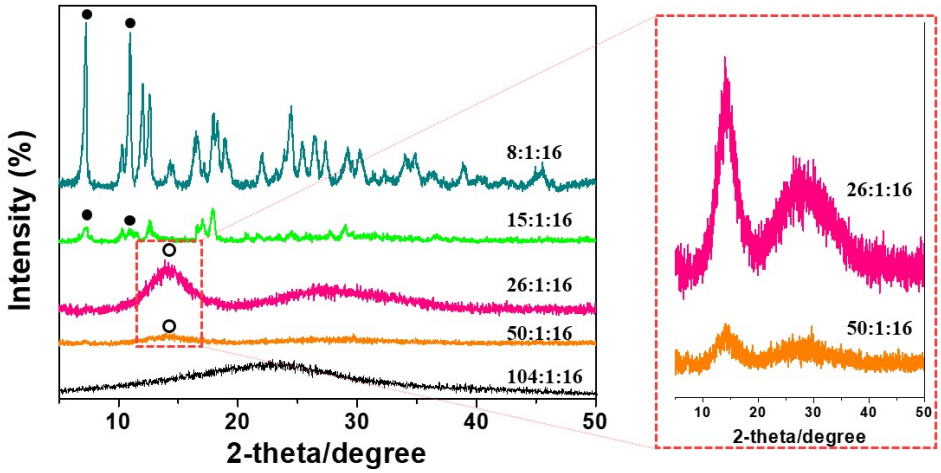

Fig. S4. X-ray diffraction patterns for investigation of crystallinity of flow synthesized Pdop@enzyme@ZIF-8 with different Pdop:enzyme:ZIF-8 ($Zn^{2+}$and 2-MIM) flow ratio (black line; 104: 1: 16, orange line; 50: 1: 16, pink line; 26: 1: 16, green line; 15: 1: 16 and cyan line; 8: 1: 16). (●: crystal ZIF-8 peak, ○: amorphous ZIF-8 peak).

Pdop flow rates-dependent formations of the crystal ZIF-8, amorphous ZIF-8, and non-ZIF-8. At the flow condition 8:1:16 with the highest degree of interfacial diffusion, the core@shell nanoparticle (NPs) became a crystalline structure with well-developed (011), (002), (112), and (022) peaks. As the interfacial diffusion (15:1:16 condition) decreases, we observed a decrease in the crystalline peak (●: (011) and (002)). On the other hand, at the moderate flow condition 26:1:16, two broad peaks at 14°, ~26° were observed, which is the most likely to the characteristics of amorphous ZIF-8 structure. As decreased interfacial diffusion (50:1:16 condition), the amorphous ZIF-8 peak (○: 14°, ~26° peak) of core@shell NPs was decreased. Finally, at the flow condition 104:1:16 with the lowest diffusion rate, a non-porous structure with a single broad XRD peak was observed.

3. Urease quantification of Pdop@urease@ZIF-8

Calibration curve

Each concentration of urease solution (1 mL, 1000-50 μg/mL) in the citrate buffer (100 mM, pH 5.5) was added to a 15 mL conical tube (Falcon, Polypropylene tube) containing Bradford solution (1 mL) and UV-vis spectra were measured at 595 nm to the make calibration curve [3]. Note that, citrate buffer (pH 5.5) was used to obtain native urease from core@shell by dissolving the ZIF-8 shell.

Encapsulation efficiency of enzyme in Pdop@urease@ZIF-8 core@shell NP

To quantify the amount of urease contained in Pdop@urease@aZIF-8, 1 mg of core@shell NPs and 1 mL of citrate buffer (pH 5.5) were mixed. Then, the mixed solutions were centrifuged (13000 rpm, 3 min) to separate Pdop NPs. Then, 0.5 mL of the supernatant (urease solution) was mixed with 0.5 mL of Bradford solution, and UV-vis (595 nm) was measured. All the experiments were performed in triplicates. The encapsulation efficiency in Pdop@urease@cZIF-8 synthesized in batch: 97.1 %, Pdop@urease@cZIF-8 synthesized in flow condition C3: 97.6%, Pdop@urease@aZIF-8 synthesized in flow condition C2: 94.6 %, core@non-porous shell synthesized in flow condition C1: 0.9 %. The amount of urease in Pdop@urease@aZIF-8 synthesized in flow condition C2 was calculated to be 40.7 μg.

The enzyme encapsulation efficiency was calculated by the below equation to compare the amount of released enzyme to the total amount of enzyme in buffer used for synthesis of Pdop@urease@ZIF-8 [4].

$$Encapsulation\ efficiency\ (\%) = \frac{Amount\ of\ release\ enzyme}{Amount\ of\ supplied\ enzyme} \times 100$$

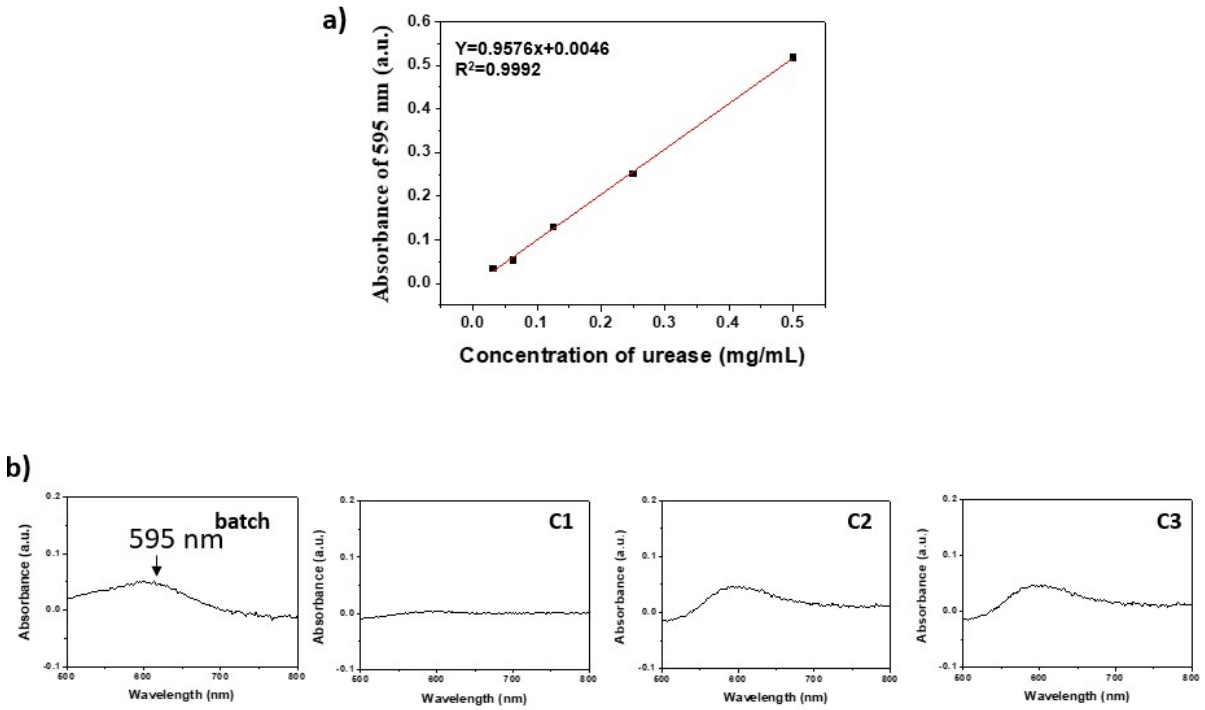

Fig. S5. a) Calibration UV absorbance (595 nm) of urease with known concentrations and b) UV-vis spectrum of the release enzymes from batch synthesized Pdop@urease@cZIF-8, flow synthesized Pdop@urease@aZIF-8 at flow conditions C1, C2 and C3 to quantify the entrapped urease on the core@shell using Bradford assay.

4. Urease activity test of Pdop@urease@ZIF-8

A solution of urea (300 mM) and phenol red (30 µL, 1 mg/mL) in PBS buffer (2.91 mL, pH 7.4) was added to a 15 mL conical tube (Falcon, Polypropylene tube). Pdop@urease@ZIF-8 suspension (120 µL) was added and the conical tube was sealed. The concentration of Pdop@urease@ZIF-8 suspension. The increase in the absorbance at 560 nm versus time (0-24 hrs) was used to measure the relative activity. The relative enzyme activity was calculated by comparing the performance of the native enzyme corresponding to the total amount of enzyme supplied for sample preparation [5], as follow:

$$\left(\frac{Ab.\,(560\ nm,\ Pdop@urease@ZIF\text{-}8)}{Ab.\,(560\ nm,\ native\ urease\ as\ total\ supplied\ amount)}\right)\times 100$$

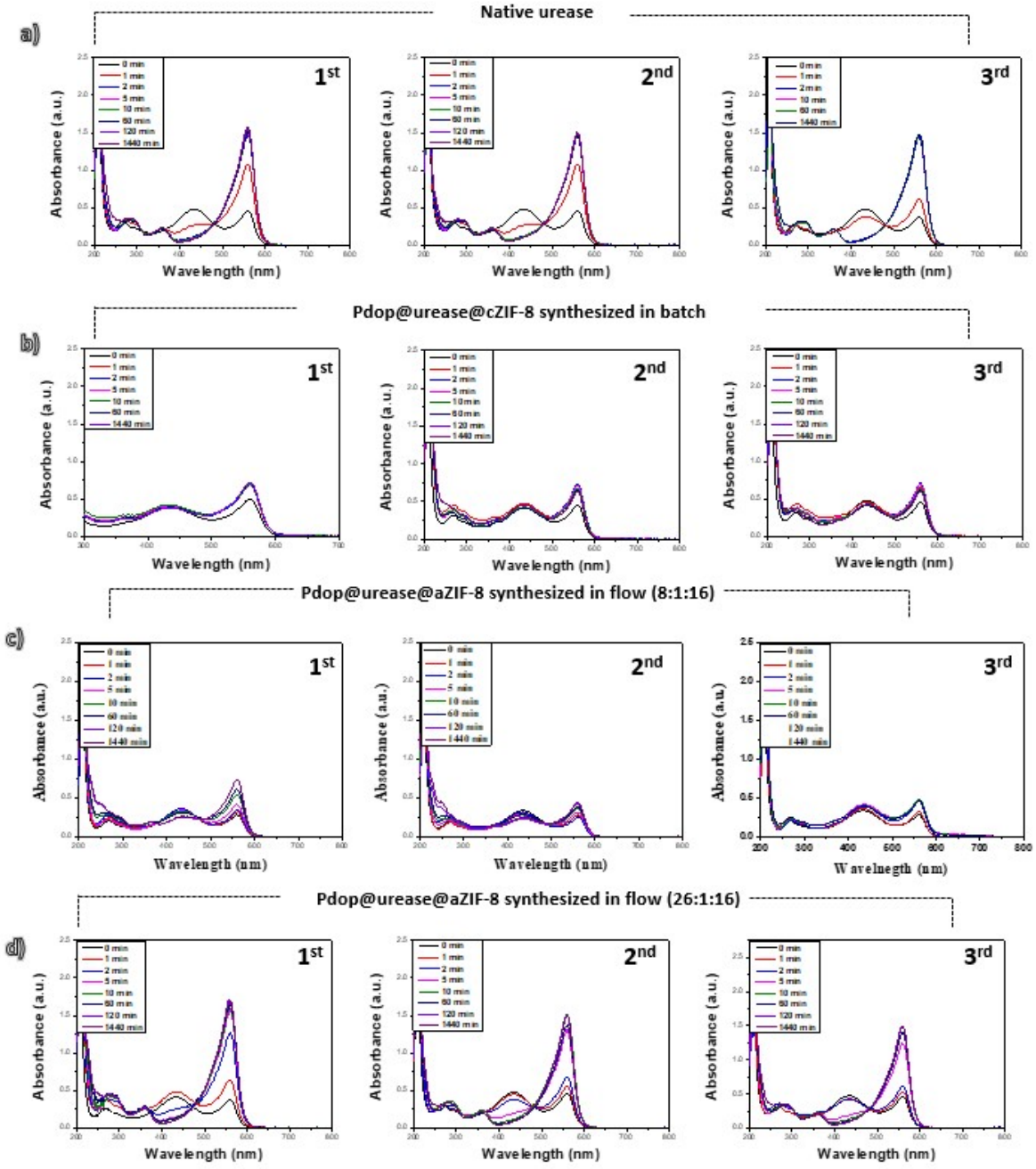

Fig. S6. UV-vis spectrum of a) native urease, b) Pdop@urease@cZIF-8 synthesized in batch, c,d) Pdop@urease@aZIF-8 with different flow conditions (Pdop: urease: ZIF-8 = 8:1:16, and 26:1:16) for comparing the relative activity.

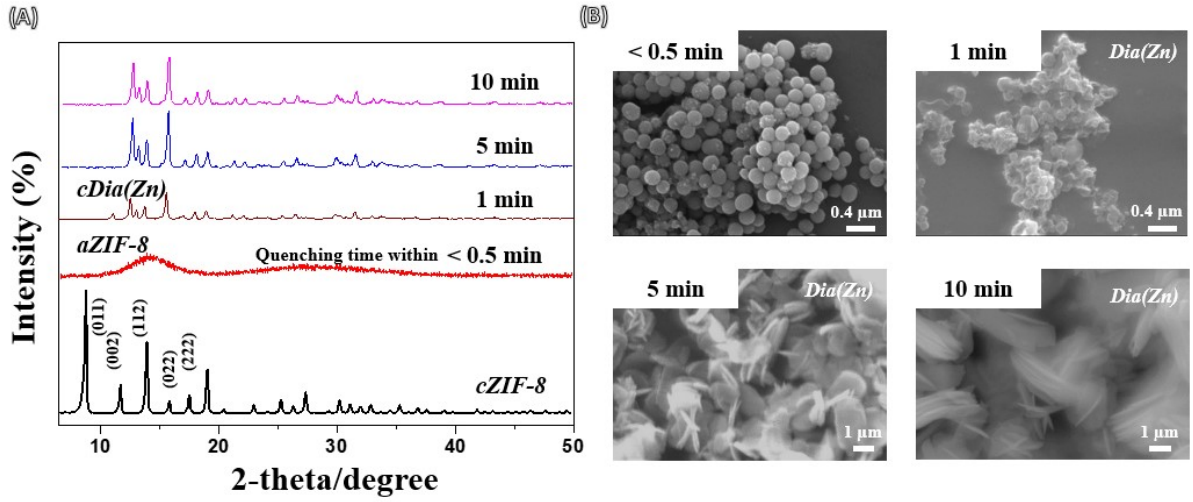

Fig. S7. (A) XRD patterns and (B) SEM images for investigation of Pdop@urease@ZIF-8 and crystalline c*Dia(Zn)* as an isomorphic Zn-MOF structures prepared at the Pdop: enzyme: ZIF-8 flow ratio (26: 1: 16) with different quenching times.

5. Photothermal performance

The aqueous dispersion of Pdop, Pdop/native urease, C-motor (Pdop@urease@cZIF-8 synthesized in batch), and A-motor (Pdop@urease@aZIF-8 synthesized in flow) were placed in a 1.5 mL EP tube (1 mL per tube) with different concentrations of 50-1600 μg/mL and exposed to an 808 nm NIR laser with irradiation (intensity: 0.2-2 W/cm^2) for 17 min. The temperatures of samples were recorded every 1 min [6].

6. Motion test of Pdop, C-motor, and A-motor

2D motion tracking was recorded using optical video (pco.edge sCMOS camera with NIS-Elements BR 4.500.00 64 bit) as reported method [7]. The movement videos of the nanoparticles (10 particles) were taken through using an inverted microscope (Nikon Ti-DH, 20 fps) equipped with a 60x microscope at room temperature. Video analysis and modeling tool Tracker 5.1.3 Program was used to analyze the trajectories, and calculated the mean squared

displacement (MSD) and average velocity by using the synthesized nanoparticles. The biocatalytic motion of nano-motors (concentration: 400 μg/mL) was monitored by transferring the sample to an aqueous urea solution (300 mM) for 20 sec. Moreover, enhanced thermo biocatalytic motion was also tested in the condition of urea (300 mM) and NIR-on (0.8 W/cm^2). MSD was calculated by the following formula. $MSD(\Delta t) = \ < r2(\Delta t) >= \left\langle \frac{1}{N}\sum_{i=0}^{N}[r_i(t) - r_i(t+\Delta t)]^2 \right\rangle$ N: number of particles, $r_i(t) - r_i(t+\Delta t)$ vector distance traveled by a particle over the time (Δt) interval. The speed of the particles was calculated by fitting MSDs from individual trajectories (up to 2 sec) to a quadratic equation of the form $MSD(\Delta t) = 4D_t + v^2t^2$ and averaging between all particles.

7. Stability test of Pdop/native urease and A-motor

To evaluate the stability of nanoparticles (Pdop/native urease and A-motor), biocatalytic-motion and photothermal test were sequentially performed with the urea (0, 300 mM) solution and NIR (2 W/cm^2) for 5 days. First, nanoparticles (1mL, 400 μg/mL) immerged in the urea solution for 10 min to test the stability of motion. Subsequently, the above solution was exposed by NIR for 5 min to test the stability of photothermal ability. Then, the above tested solution was stored at room temperature for 23 hrs 30 min without a washing step. Before the next stability test, the tested solutions were centrifuged 3 times at 3000 rpm for 10 min and re-dispersed in urea (0, 300 mM) and then, above experiments were carried out for 5 days [8].

8. Cytotoxicity assay

The biocompatibility of the synthesized nano-motors were analyzed with fibroblast cells (NIH3T3). First, different concentrations of the nanoparticle (100 μg/mL, 200 μg/mL,

400 μg/mL) were prepared in DMEM (Dulbecco's Modified Eagle Medium) supplemented with 10 % fetal bovine serum (FBS). Then the solutions were separately added into 96 well plate containing NIH3T3 cells at concentration of $2x10^4$ cells per well. After 24 hrs of incubation in CO_2 incubator at 37 ℃, MTS assay was performed. Note that, all the experiments were performed triplicate.

9. Preparation of fluorophore-labeled enzyme (urease and proteinase K)

Proteinase K and urease were separately prepared by labeling each protein with Cy5 and Cy5.5 fluorophores. Briefly, the enzyme (1 mg/mL) in PBS (1×; pH 7.4) was added to 4 μL of the sulfo-fluorophore-NHS ester (1 mM; Lumiprobe) and incubated for 30 min. Then, the modified enzymes were purified three times with PBS through a 100 kDa filter (Millipore) with centrifugation at 3600 rpm for 10 min.

10. Cellular uptake analysis and photothermal therapy

For the labeling of the nanoparticles, rhodamine B (5 mg) and Pdop (4 mg) were stirred with 10 mL D.I. water at room temperature for 12 hrs in brown-vial. After that, the result solution was centrifuged at 3000 rpm for 10 min and finally dried in vacuum at room temperature for 24 hrs. Fluorescence labeled polydopamine nanoparticles (Pdop-rhodamine B) and nano-motors (A-motor-rhodamine B) were separately prepared in McCoy's 5a Medium at concentration of 400 μg/mL. T-24 cells that were cultured in 24 well plates at concentration of $4x10^5$ were co-incubated either with Pdop or nano-motors for 24 hrs. The cellular uptake of the nanoparitcles or nano-motors were examined with fluorescent microscope. For better visualization of the location of the Pdop and nano-motor, cell cytoplasm and cell nucleus were stained with calcein AM and DAPI.

Photothermal therapeutic potential of the synthesized Pdop and nano-motor was further assessed via irradiation of NIR laser (2W/cm^2) to the T-24 cells that have uptaken Pdop or nano-motors. Note that, T-24 cells that were untreated of Pdop or nano-motors were used as control; and they were also irradiated with NIR. After 5 min irradiation of NIR laser, live cells were stained with calcein AM. Again, all the experiments were performed in triplicate.

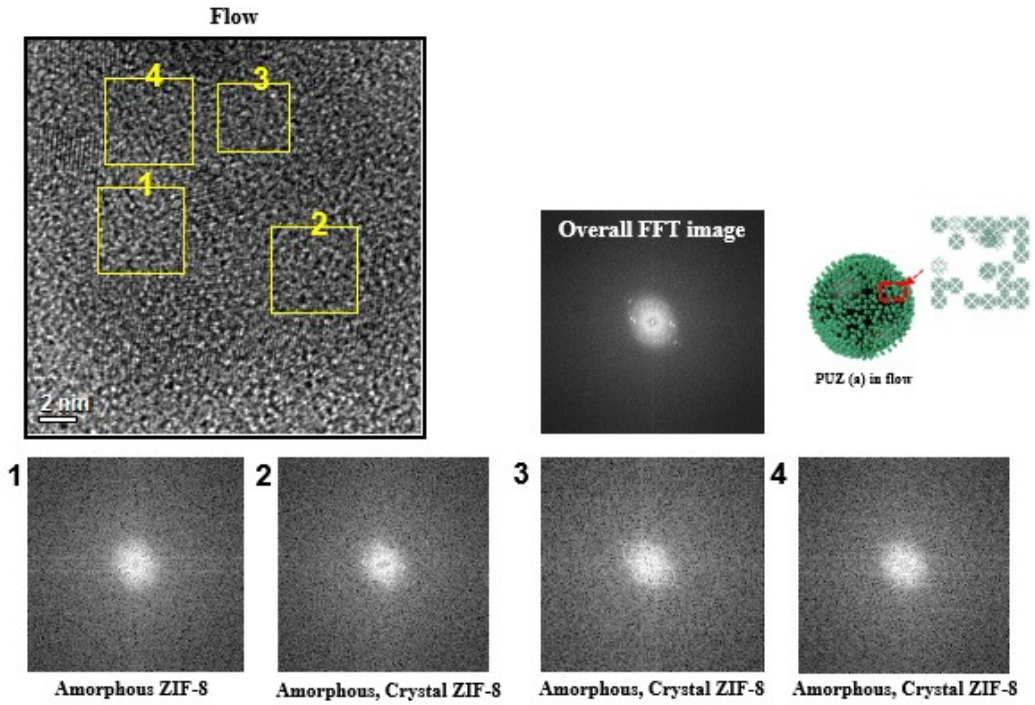

Fig. S8. HRTEM image and FFT of Pdop@enzyme@aZIF-8 synthesized in flow. The corresponding FFT show crystal and amorphous structure in Pdop@enzyme@aZIF-8 .

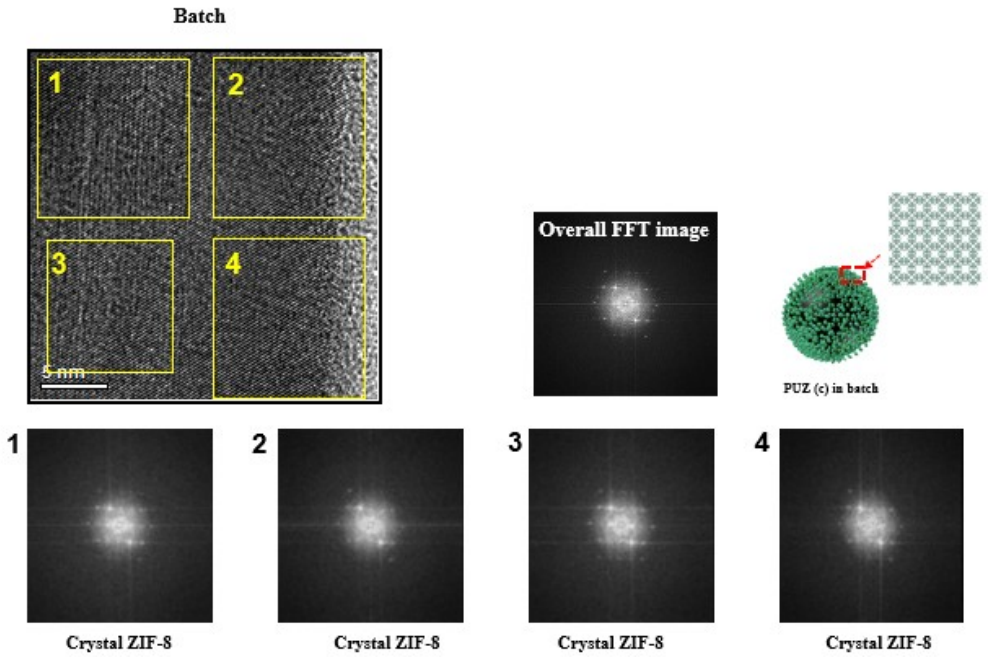

Fig. S9. HRTEM image and FFT of Pdop@enzyme@cZIF-8 synthesized in batch. The corresponding FFT show crystallinity in Pdop@enzyme@cZIF-8.

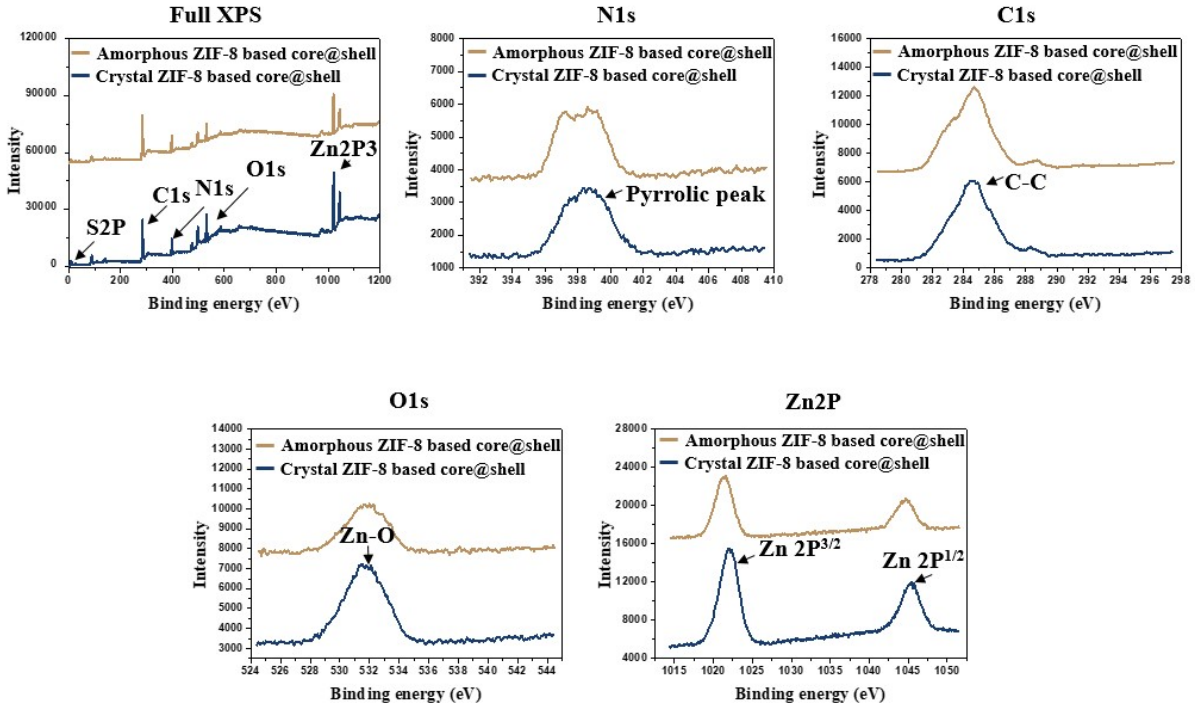

Fig. S10. XPS full, N1s, C1s, O1s and Zn2P spectra of Pdop@urease@ZIF-8 nanoparticles synthesized in flow (amorphous ZIF-8) and in batch (crystal ZIF-8).

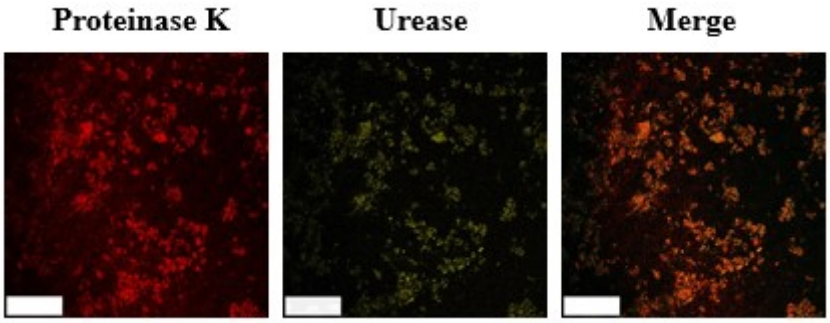

Fig. S11. Dual encapsulated enzyme (red: proteinase K and green: urease) on nano-motor (Pdop@urease@aZIF-8). For demonstration, co-entrapment of proteinase K and urease were each labeled with different fluorescent dyes (red and green) respectively. The dual color images of two enzymes were observed.

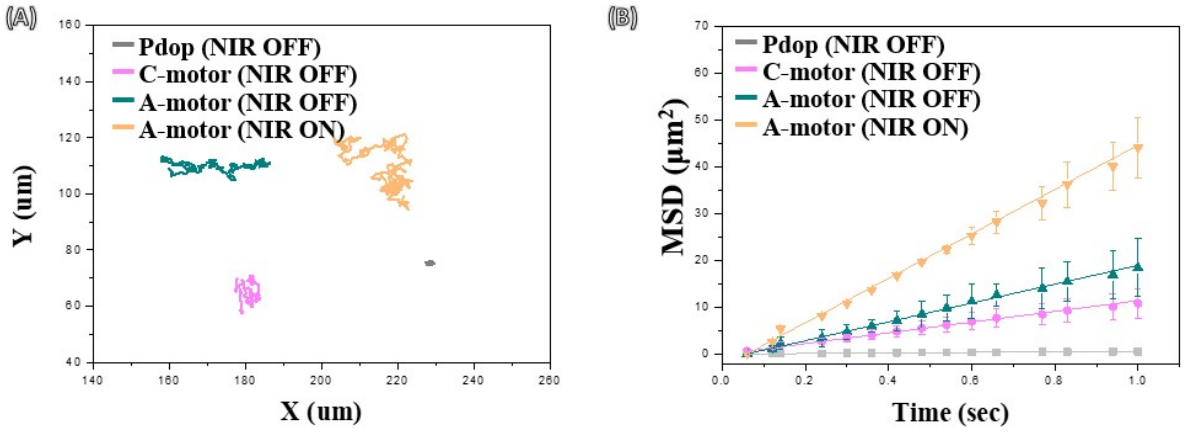

Fig. S12. Biocatalytic motion analysis of A-motor nanoparticle. (A) Swimming trajectories of Pdop, C-motor (Pdop@urease@cZIF-8, NIR-off), A-motor (Pdop@urease@aZIF-8, NIR-off), and A-motor (Pdop@urease@aZIF-8 NIR-on) under simulated urine conditions (urea, 300 mM) with and without low-intensity NIR (808 nm, 0.8 W/cm^2). (B) Mean square displacement (MSD) of Pdop, C-motor (Pdop@urease@cZIF-8, NIR off), A-motor (Pdop@urease@aZIF-8

NIR on and off) as nano-motors under simulated urine (300 mM, urea) with and without low-intensity NIR (808 nm, 0.8 W/cm^2).

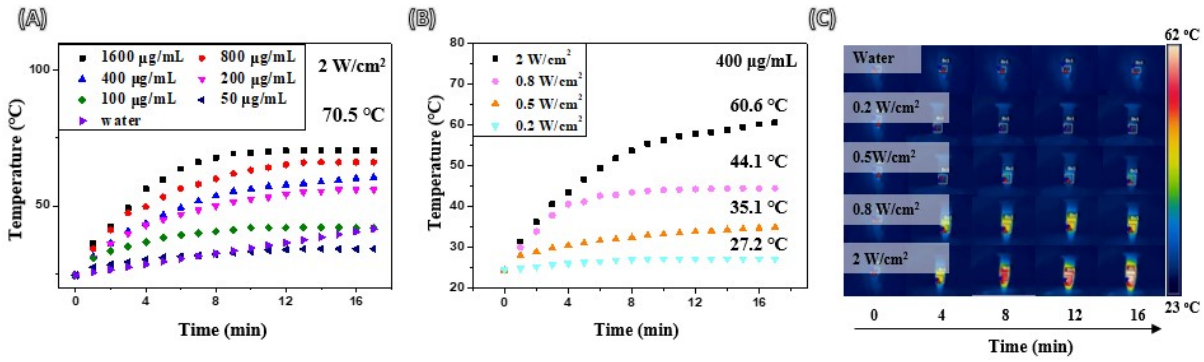

Fig. S13. (A) Temperature elevation curves for 1020 sec of A-motor with different concentration (0-1600 μg/mL) upon irradiation (808 nm, 2W/cm^2) and (B) with different NIR intensities (0.2-2 W/cm^2). (C) Infrared thermal images at different NIR intensities (0-2 W/cm^2). Superior photothermal properties of flow-synthesized A-motor nanoparticle to other.

The PTT effect of A-motor was determined by analyzing the temperature changes under different A-motor concentrations (0–1,600 μg/mL) and NIR intensities (0.2–2 W/cm^2) (**Fig. S13a**). The temperature of the solution plateaued after approximately 8–12 min and reached 70.5 °C at the highest concentration. Moreover, this temperature rise could be controlled by the NIR intensity. High intensity NIR (2 W/cm^2) was effective for killing cancer cells and low-intensity NIR (0.8 W/cm^2) was effective for increasing urease activity (**Fig. S13b**). In addition, the thermal contrast of Pdop@urease@aZIF-8 resulted in good IR thermal imaging properties; therefore, this nano-motor can also be applied to photothermal imaging (**Fig. S13c**).

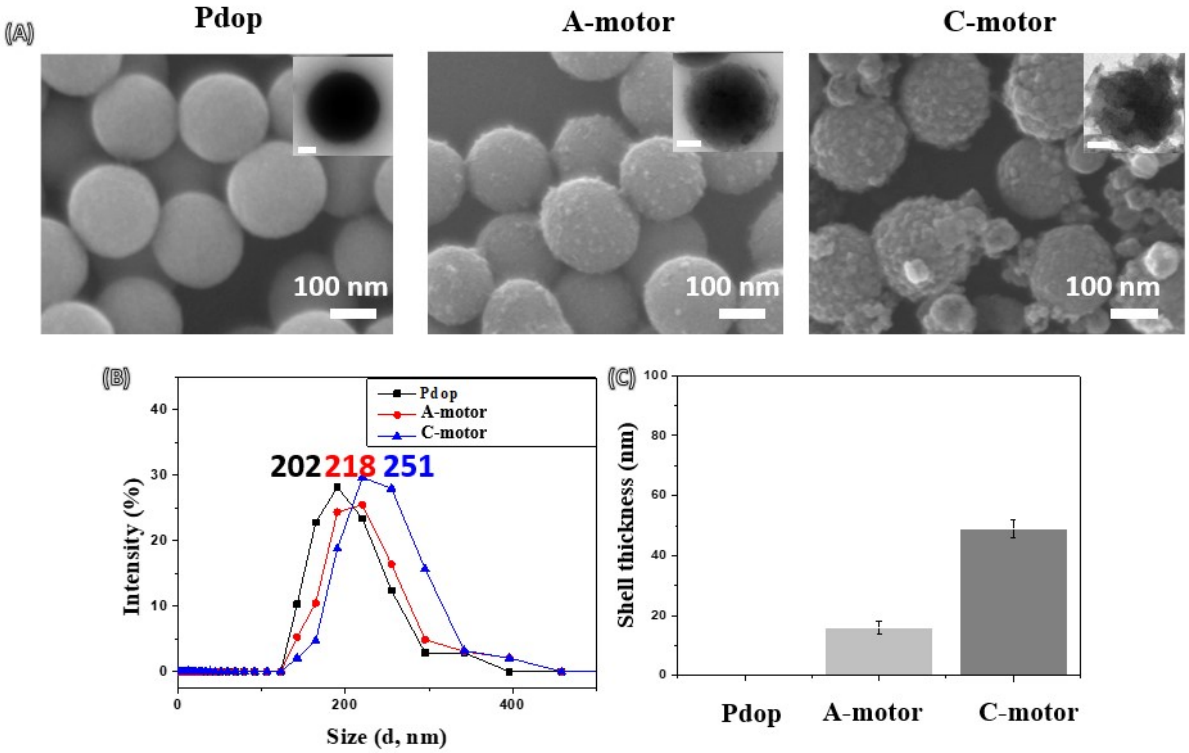

Fig. S14. (A) SEM and TEM images (inset images) and, (B) DLS, and (C) graph of shell thickness of Pdop, A-motor, and C-motor to confirm shell thickness. (inset scale bar: 50 nm)

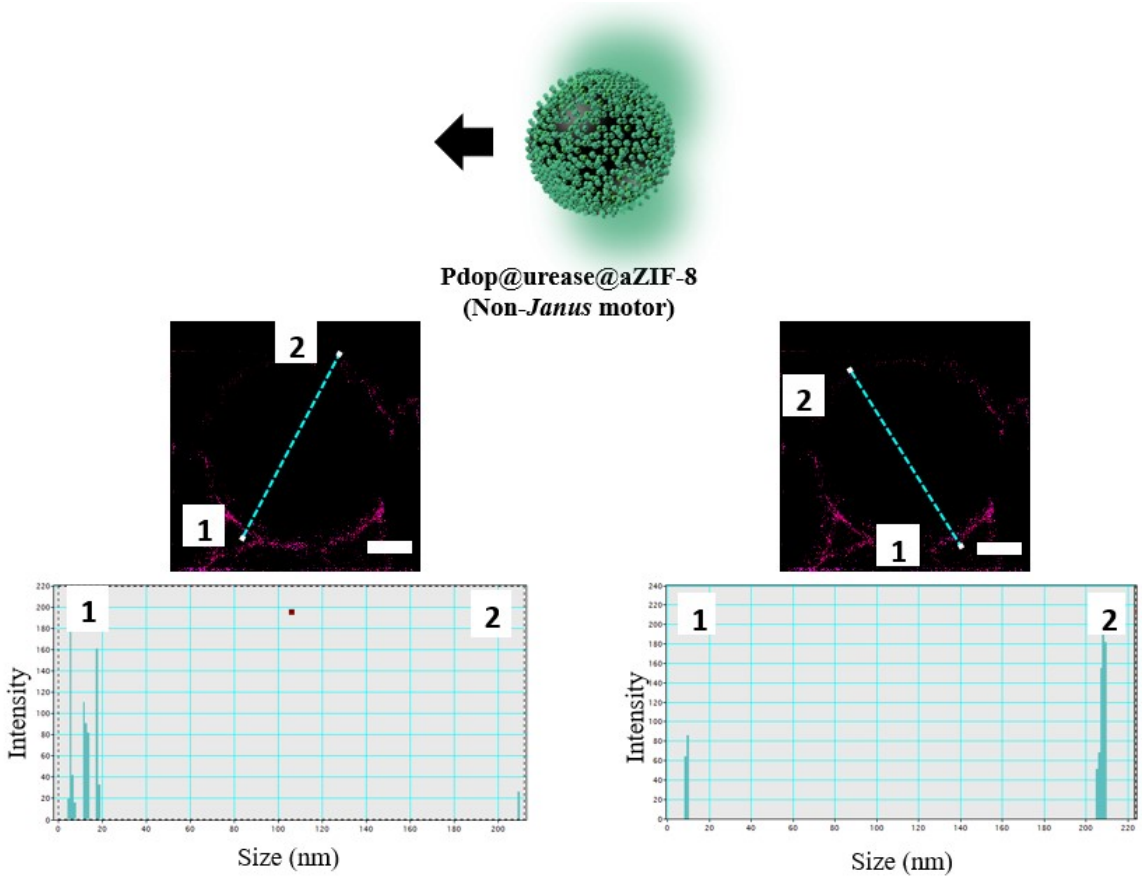

Fig. S15. Electron energy loss spectroscopy (EELS) mapping images (scale: 50 nm, purple color: urease) and EELS line scan data of A-motor (Pdop@urease@aZIF-8).

To confirm whether the nano-motor can show enhanced Brownian motion even though A-motor was a non-*Janus* motor, the enzyme distribution and the quantity of the nano-motor were confirmed by ELLS line scanning. Enhanced movement due to the asymmetrical distribution of enzymes on the non-*Janus* nano-motor surface has already been reported in many publications [9,10]. Although Pdop@urease@aZIF-8 was also a non-*Janus* nano-motor, the distribution of the synthesized urease showed a non-linear coverage, and each amount distributed was also different.

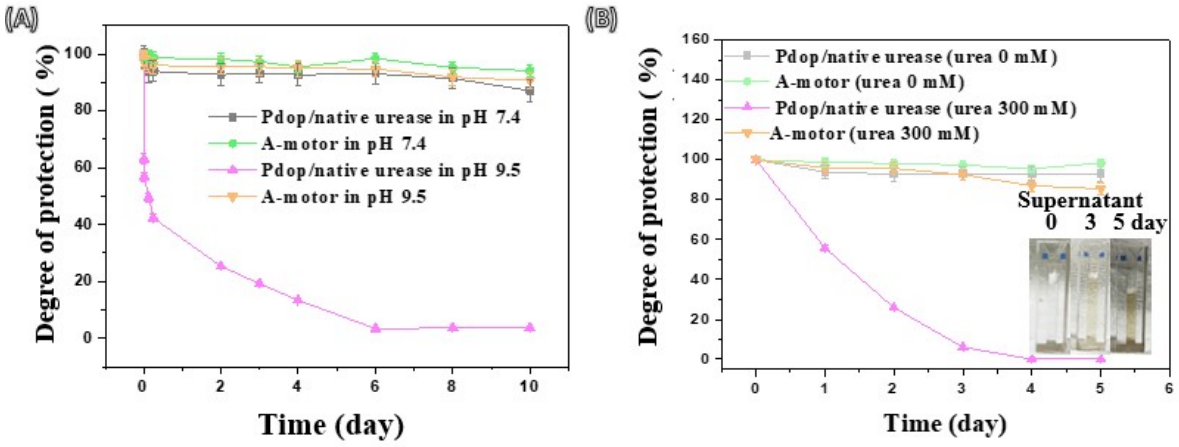

Fig. S16. Degree of protection of Pdop/native urease (gray and purple color) and A-motor (green and orange color) with different (A) pH value (neutral pH, 7.4 and alkali pH, 9.5) and (B) urea concentrations (0 and 300 mM).

Before the degradation test of Pdop by ammonia product of urease and urea reaction, the degradation test of pdop by pH 9.5 was carried out. At pH 7.4, which was a neutral solution, there was no degradation of Pdop/native urease and A-motor for 5 days, and it had no effect on the temperature elevation. In a solution with pH 9.5, Pdop/native urease was degraded and also influenced the temperature elevation. On the other hand, A-motor minimized the effect of temperature elevation due to the prevention of the degradation of aZIF-8.

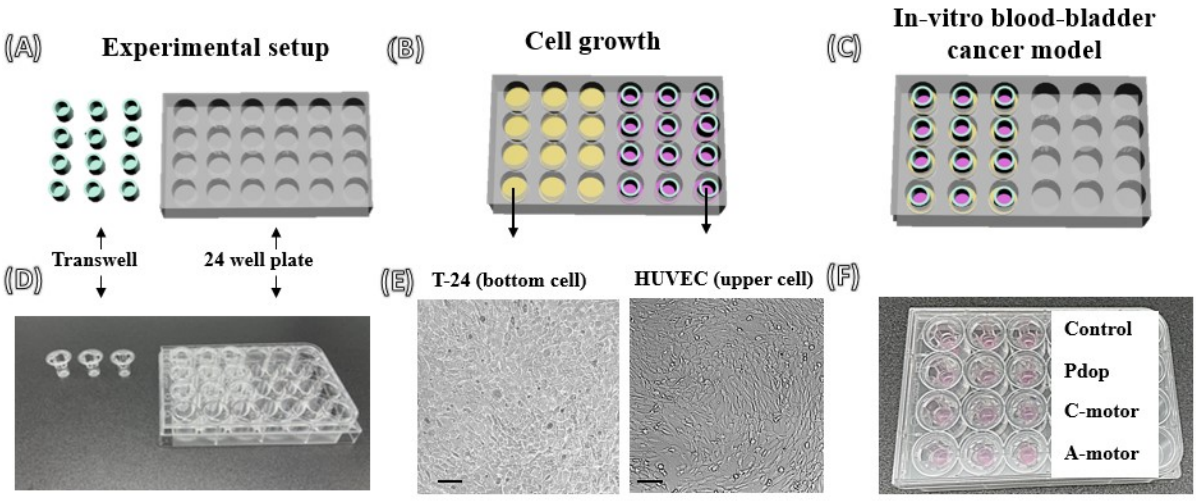

Fig. S17. Schematic illustration of (A) experimental set-up, (B) separate cell culture of T-24 and HUVEC, and (C) in-vitro blood-bladder cancer model. (D) Photograph of transwell and 24 well plate. (E) microscope images of T-24 (24 well plate part) and HUVEC (transwell part) cells forming a confluent monolayer. (F) Photograph of formation of in-vitro blood-bladder cancer model for sequential transmigration and photothermal therapy test of Pdop, C-motor, and A-motor for bladder cancer cell under simulated condition (urea, 300 mM)

10. 2D cellular models for studying transmigration and sequential photothermal therapy (PTT) of nano-motors.

In vitro bladder model that mimics the interface between bladder tissue and blood vessel tissue were developed by following a previous report with slight modification [11]. Briefly, $2x10^4$ HUVEC cells that were dispersed in EGM (endothelial cell growth media) were seeded and cultured onto the transwell membrane (pore size of 8 μm). Once confuent monolayer of HUVEC tissue was formed, the HUVEC layer was relocated at the top of the 24 well plate containing $2x10^4$ of T-24 cells in McCoy's 5a Medium **(Fig. S14)**. Then, 400 μg/ml of Pdop, C-motors or A-motors with urea (300 mM) were separately introduced to the HUVEC cells allowing transfer of the nanoparticles or nano-motors across the HUVEC layer to T-24 cells.

After incubation in CO_2 incubator at 37 ℃ for 24 hrs, NIR laser (2 W/cm^2) was irradiated to the T-24 cells for 5 min. Cells were stained with Calcein AM and Hoechst. Note that, T-24 cells that were untreated of Pdop or nano-motors were used as control **(Fig. S14, S15)**.

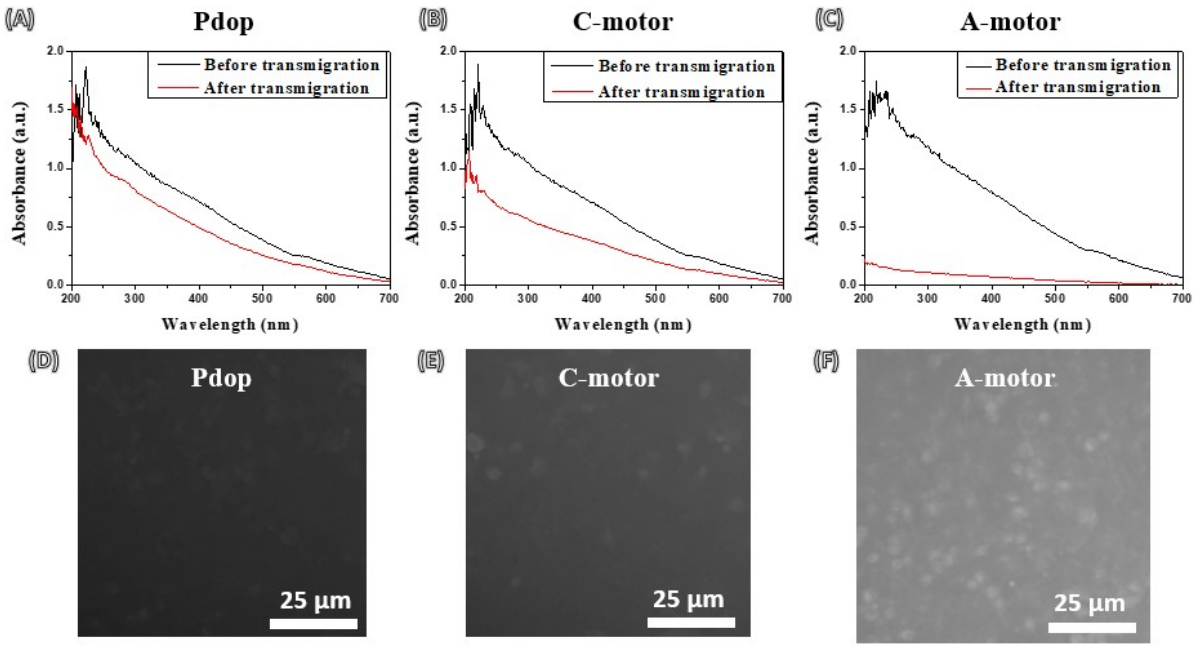

Fig. S18. UV-vis absorbance data of (A) Pdop, (B) C-motor, and (C) A-motor in the upper cell membrane before and after transmigration. Fluorescent image of (D) Pdop, (E) C-motor and (F) A-motor in the lower membrane after transmigration.

References

1 V. Viktorov, M. R. Mahmud and C. Visconte, *Eng. Appl. Comput. Fluid Mech.*, 2016, **10**, 183–193.

2 G. N. Ahn, T. Yu, H. J. Lee, K. W. Gyak, J. H. Kang, D. You and D. P. Kim, *Lab Chip*, 2019, **19**, 3535–3542.

3 P. Falcaro, F. Carraro, M. D. J. Velásquez-Hernández, E. Astria, W. Liang, L. Twight,

C. Parise, M. Ge, Z. Huang, R. Ricco, X. Zou, L. Villanova, C. O. Kappe and C. Doonan, *Chem. Sci.*, 2020, **11**, 3397–3404.

4 M. Chaturvedi, Y. Molino, B. Sreedhar, M. Khrestchatisky and L. Kaczmarek, *Int. J. Nanomedicine*, 2014, **9**, 575–588.

5 K. Liang, C. J. Coghlan, S. G. Bell, C. Doonan and P. Falcaro, *Chem. Commun.*, 2016, **52**, 473–476.

6 H. Zhuang, H. Su, X. Bi, Y. Bai, L. Chen, D. Ge, W. Shi and Y. Sun, *ACS Biomater. Sci. Eng.*, 2017, **3**, 1799–1808.

7 D. Vilela, A. C. Hortelao, R. Balderas-Xicohténcatl, M. Hirscher, K. Hahn, X. Ma and S. Sánchez, *Nanoscale*, 2017, **9**, 13990–13997.

8 B. K. Kaang, N. Han, H. J. Lee and W. S. Choi, *ACS Appl. Mater. Interfaces*, 2018, **10**, 1113–1124.

9 T. Patiño, N. Feiner-Gracia, X. Arqué, A. Miguel-López, A. Jannasch, T. Stumpp, E. Schäffer, L. Albertazzi and S. Sánchez, *J. Am. Chem. Soc.*, 2018, **140**, 7896–7903.

10 A. C. Hortelao, R. Carrascosa, N. Murillo-Cremaes, T. Patino and S. Sánchez, *ACS Nano*, 2019, **13**, 429–439.

11 M. Wan, Q. Wang, X. Li, B. Xu, D. Fang, T. Li, Y. Yu, L. Fang, Y. Wang, M. Wang, F. Wang, C. Mao, J. Shen and J. Wei, *Angew. Chemie*, 2020, **132**, 14566–14573.